

Double-diffusive transport in multicomponent vertical convection

Christopher J. Howland,^{1,*} Roberto Verzicco,^{2,3,1} and Detlef Lohse^{1,4,†}

¹*Physics of Fluids Group, Max Planck Center for Complex Fluid Dynamics,
MESA+ Institute and J.M. Burgers Centre for Fluid Dynamics,
University of Twente, P.O. Box 217, 7500AE Enschede, Netherlands*

²*Dipartimento di Ingegneria Industriale, University of Rome ‘Tor Vergata’,
Via del Politecnico 1, Roma 00133, Italy*

³*Gran Sasso Science Institute, Viale F. Crispi, 7, 67100 L’Aquila, Italy*

⁴*Max Planck Institute for Dynamics and Self-Organization,
Am Fassberg 17, 37077 Göttingen, Germany*

(Dated: July 20, 2022)

Abstract

Motivated by the ablation of vertical ice faces in salt water, we use three-dimensional direct numerical simulations to investigate the heat and salt fluxes in two-scalar vertical convection. For parameters relevant to ice-ocean interfaces, we observe that the salinity field drives the convection and that heat is essentially transported as a passive scalar. By varying the diffusivity ratio of heat and salt (the Lewis number Le), we identify how the different molecular diffusivities affect the scalar fluxes through the system. Away from the walls, we find that the heat transport is determined by a turbulent Prandtl number of $Pr_t \approx 1$ and that double-diffusive effects are practically negligible. However, the difference in molecular diffusivities plays an important role close to the boundaries. In the (unrealistic) case where salt diffused faster than heat, the ratio of fluxes would scale as $Le^{1/3}$, consistent with classical nested scalar boundary layers. However, in the realistic case of faster heat diffusion (relative to salt), we observe a transition towards a $Le^{1/2}$ scaling of the ratio of the fluxes. This coincides with the thermal boundary layer width growing beyond the thickness of the viscous boundary layer. We compare our results to similar studies of sheared and double-diffusive flow under ice shelves, and discuss the implications for fluxes in large-scale ice-ocean models.

I. INTRODUCTION

Over the last century, the loss of land-based ice from the Greenland and Arctic ice sheets has contributed significantly to sea level rise, and the rate of this mass loss has increased up to sixfold over the last 40 years [1, 2]. Future projections from an ensemble of climate models indicate that this rate is set to increase further over the coming century for a range of emissions scenarios, endangering many regions to coastal flooding [3–5]. Despite the importance of these projections, the complexity of the climate system introduces significant uncertainty regarding the magnitude of future sea level rise. One key source of uncertainty arises from the parameterisation of melting at the ice-ocean interface [6]. These parameterisations range in complexity from simple linear or quadratic dependences on the ambient ocean temperature to buoyant plume models. To reduce the uncertainty associated with such parameterisations, it is important to understand the physical mechanisms driving the

* c.j.howland@utwente.nl

† d.lohse@utwente.nl

ice ablation, particularly for regions of relatively warm, salty water where ice retreat is fastest.

From a fundamental physical perspective, the melt rate of ice in salt water depends only on the gradients of temperature and concentration at the ice interface, which determine the diffusive fluxes of heat and salt towards the ice [7, 8]. A common assumption in melt parameterisations is that the fluxes are determined by the velocity of the water adjacent to the ice, with the flow taking the form of a classical shear-driven turbulent boundary layer [9]. In that case, both scalars (heat and salt) are transported passively. However, recent observational and experimental work points to buoyancy playing an important role in scenarios where the ambient currents are weak. Close to the ice-ocean interface, buoyancy perturbations are dominated by differences in the salt concentration of the water rather than temperature. For horizontal ice faces, this creates a stable density stratification as the cold, fresh meltwater remains in contact with the ice. This fresh layer can then undergo double-diffusive convection due to the differing diffusivities of heat and salt [10], leading to observations where the melt rate is independent of the ambient flow velocity [11]. At steeply sloped ice faces, found at tidewater glaciers [12] and on the underside of ice shelves [13], the fresh meltwater instead forms a rising plume [14]. Experiments suggest that the melt rate in this case is also independent of the flow velocity, and that theory for vertical surfaces can easily be applied to those with steep slopes [15, 16].

One extreme difficulty for modelling the melt rate of ice in salt water is that the diffusive boundary layers controlling the heat and salt fluxes are on the millimetre scale. These boundary layers are extremely difficult to analyse experimentally or in the field, but have recently become accessible through numerical simulations. Resolving the boundary layers allows us to directly measure the diffusive fluxes at the ice interface, which are not only coupled to the melt rate but also to the local melting point of the ice, which depends on the local salinity [8]. Two recent studies have found the presence of stable buoyancy gradients to modify the ratio of salt flux to heat flux at the interface when compared to purely shear-driven systems [17, 18]. Through the coupled boundary condition at the ice-water interface, this ratio in turn modifies the melt rate.

The physical mechanism underlying these changes in flux ratio is however complex. In the case of a horizontal ice surface, simulations of diffusive convection beneath a melting ice face [19] have found a non-trivial dependence of the flux ratio on the ratio of heat diffusivity

to salt diffusivity, known as the Lewis number $Le = \kappa_T/\kappa_C$. However, for vertical ice faces, the appropriate flux ratio is completely unknown, with proposed theory [15] and common parameterisations [20] in disagreement.

To gain physical insight into the mechanisms determining the flux ratio in such convective boundary layers, in this paper we perform direct numerical simulations of a highly simplified setup. We consider the vertical convection (VC) flow in an infinite vertical channel between two stationary walls held at fixed (but different) temperatures and salt concentrations. The fixed scalar values are justified by the results of [21], where the interfacial values of temperature and salinity at a melting ice face reach a constant value as the flow develops a statistically steady state. Rather than fixing the fluid properties to realistic values, in order to better understand the physical mechanisms, we vary the Schmidt number and Lewis number and systematically investigate how the fluxes depend on the dimensionless control parameters of the system. This study builds on our previous work on VC at high Prandtl number [22]. As in that study, we use a multiple-resolution technique to perform large three-dimensional simulations with low-diffusivity scalars at a reduced computational cost. Unlike some previous studies of multicomponent convection in a vertical channel [23], we neglect the effect of any mean ambient stratification. In the motivating example of convection at a tidewater glacier face, the buoyancy perturbations in the boundary layer are significantly greater than the buoyancy differences in the ambient, so we do not expect detrainment from the wall and layering due to stratification. The flow we consider is turbulent due to the strong buoyancy forcing, and we are far from the marginal stability curves identified for this problem [24, 25].

The rest of the paper is organised as follows. We describe the governing equations, control parameters, and numerical methods used in section II. This is followed by presentation of the results where we highlight the effect of thermal buoyancy on the flow (III A), the global heat flux and how it is related to the salt flux (III B), the widths of the scalar boundary layers (III C), and the turbulent diffusivity away from the walls (III D). Finally, we conclude and discuss our results in the context of ice-ocean interfaces in section IV.

II. NUMERICAL METHODS AND SIMULATION SETUP

We consider the fluid flow inside a vertical channel of width H , with fixed values of temperature T and solute concentration C at each wall. These impose a temperature difference ΔT and a concentration difference ΔC between the walls, where the density ratio $R_\rho = \beta_T \Delta T / \beta_C \Delta C = 0.02$ is fixed in all the simulations. Here, β_T is the isobaric thermal expansion coefficient and β_C is the haline contraction coefficient. Following the Oberbeck–Boussinesq approximation, density differences obey a linear equation of state

$$\rho = \rho_0 (1 - \beta_T(T - T_0) + \beta_C(C - C_0)), \quad (1)$$

and are only non-negligible in the buoyancy term of the momentum equations. We therefore consider incompressible flow such that the velocity field \mathbf{u} satisfies $\nabla \cdot \mathbf{u} = 0$ and conservation of momentum. The temperature and concentration fields satisfy advection-diffusion equations, such that the full set of governing equations reads

$$\frac{\partial \mathbf{u}}{\partial t} + (\mathbf{u} \cdot \nabla) \mathbf{u} = -\rho_0^{-1} \nabla p + g(\beta_T T - \beta_C C) \hat{\mathbf{z}} + \nu \nabla^2 \mathbf{u}, \quad (2)$$

$$\frac{\partial T}{\partial t} + (\mathbf{u} \cdot \nabla) T = \kappa_T \nabla^2 T, \quad (3)$$

$$\frac{\partial C}{\partial t} + (\mathbf{u} \cdot \nabla) C = \kappa_C \nabla^2 C. \quad (4)$$

Here g is gravitational acceleration, which acts in the z -direction, ν is the kinematic viscosity, and κ_T and κ_C are the molecular diffusivities of heat and salt respectively. We consider a domain of length $8H$ in the vertical direction (z) and $4H$ in the spanwise direction (y), and impose periodic boundary conditions along these axes, as in our previous single component study [22].

Since there is no flow imposed in this system, its dynamics are uniquely determined by four dimensionless control parameters. These are the aforementioned density ratio

$$R_\rho = \frac{\beta_T \Delta T}{\beta_C \Delta C}, \quad (5)$$

along with the Rayleigh number, Schmidt number and Lewis number

$$Ra = \frac{g \beta_C H^3 \Delta C}{\nu \kappa_C}, \quad Sc = \frac{\nu}{\kappa_C}, \quad Le = \frac{\kappa_T}{\kappa_C}. \quad (6)$$

We take the Rayleigh number to be based on the buoyancy of the concentration field since the density ratio is small and thus the buoyancy is mainly due to concentration differences.

Instead of the Rayleigh number, one could also characterise the dynamics in terms of the Grashof number $Gr = Ra/Sc$ which is equivalent to the square of a Reynolds number based on the free-fall velocity scale $U_f = \sqrt{g\beta_C H \Delta C}$ and the plate separation H . Prescribing the Schmidt number and Lewis number in turn fixes the Prandtl number $Pr = \nu/\kappa_T$.

We solve the governing equations (2)-(4) numerically using our in-house Advanced Finite-Difference (AFiD) code. Spatial derivatives are approximated by central second-order accurate finite differences, a Crank–Nicolson scheme is used to time-step the wall-normal diffusive terms, and a third-order Runge–Kutta scheme is used for all other terms following [26, 27]. The slower diffusing scalar field is evolved on a higher resolution grid than the grid on which all other flow variables are stored. We use tricubic Hermite interpolation between the two grids to compute the scalar advection and buoyancy terms following ref.[28]. Grid stretching is used in the wall-normal direction to resolve the thin diffusive boundary layers, whereas grid spacing is uniform in the y and z directions. Since the flow is anisotropic and dominated by thin plumes ejected from the boundary layers, the Batchelor scale is not a reliable estimate of the required resolution for each state variable [29]. We ensure resolution of the flow fields through a statistical convergence test, and by inspection of the power spectrum tails for both the velocity and scalar fields.

The input parameters for the numerical simulations are shown in table I. We perform three sets of simulations, in which the Grashof number is always fixed at $Gr = 10^6$. In the first, labelled A10 in table I, we fix $Sc = 10$ and vary the Lewis number between 0.1 and 10. We then fix $Sc = 100$ for the second set (A100), varying the Lewis number between 10 and 100. Finally, we consider two simulations (set P) where the density ratio is set to zero such that the temperature field is advected as a passive scalar. Simulation A10L10 is initialised with linear temperature and salinity profiles with small-amplitude white noise to trigger the transition to turbulence before evolving to a statistically steady state. All other simulations use the final state of that simulation as an initial condition to reduce the time needed to reach a steady state. The simulations are each evolved for 300 free-fall time units (H/U_f) in this steady state, and any time-averaged results presented below are averaged over this period.

TABLE I. Input parameters and grid resolutions for the numerical simulations.

Simulation	R_ρ	Sc	Ra	Le	Pr	Base grid resolution	Refined grid resolution
A10L10	0.02	10	10^7	10	1	$192 \times 512 \times 1024$	$384 \times 1024 \times 2048$
A10L5	0.02	10	10^7	5	2	$192 \times 512 \times 1024$	$384 \times 1024 \times 2048$
A10L2	0.02	10	10^7	2	5	$192 \times 512 \times 1024$	$384 \times 1024 \times 2048$
A10L05	0.02	10	10^7	0.5	20	$256 \times 768 \times 1536$	$384 \times 1152 \times 2304$
A10L02	0.02	10	10^7	0.2	50	$256 \times 768 \times 1536$	$512 \times 1536 \times 3072$
A10L01	0.02	10	10^7	0.1	100	$256 \times 768 \times 1536$	$512 \times 2048 \times 4096$
A100L100	0.02	100	10^8	100	1	$192 \times 512 \times 1024$	$512 \times 1536 \times 3072$
A100L50	0.02	100	10^8	50	2	$192 \times 512 \times 1024$	$512 \times 1536 \times 3072$
A100L20	0.02	100	10^8	20	5	$192 \times 512 \times 1024$	$512 \times 1536 \times 3072$
A100L10	0.02	100	10^8	10	10	$256 \times 768 \times 1536$	$512 \times 1536 \times 3072$
P10	0	10	10^7	10	1	$192 \times 512 \times 1024$	$384 \times 1024 \times 2048$
P100	0	100	10^8	100	1	$192 \times 512 \times 1024$	$512 \times 1536 \times 3072$

III. RESULTS

A. Thermal buoyancy effect

We begin our analysis by investigating whether the temperature field plays a significant role in the dynamics of the flow. We compare the results of the set P simulations, where temperature is advected as a passive scalar ($R_\rho = 0$), to their equivalent cases with $R_\rho = 0.02$. All of these cases have $Pr = 1$ fixed. In figure 1, we compare various flow profiles between these simulations. Here, we present profiles averaged in the vertical and spanwise directions, and then averaged in time, with the standard deviation in time of the mean profiles highlighted by shaded regions. Visually, the cases with $R_\rho = 0$ are very similar to those $R_\rho = 0.02$ cases where temperature plays an active role in the buoyancy.

From the mean profiles, the most significant difference emerges in the vertical velocity for $Sc = 100$, $Le = 100$. In this case the temperature field diffuses much more quickly than the concentration field, which is confined to a thin boundary layer. Close to the vertical velocity peak, the contribution of salt to the buoyancy is reduced and so despite the small

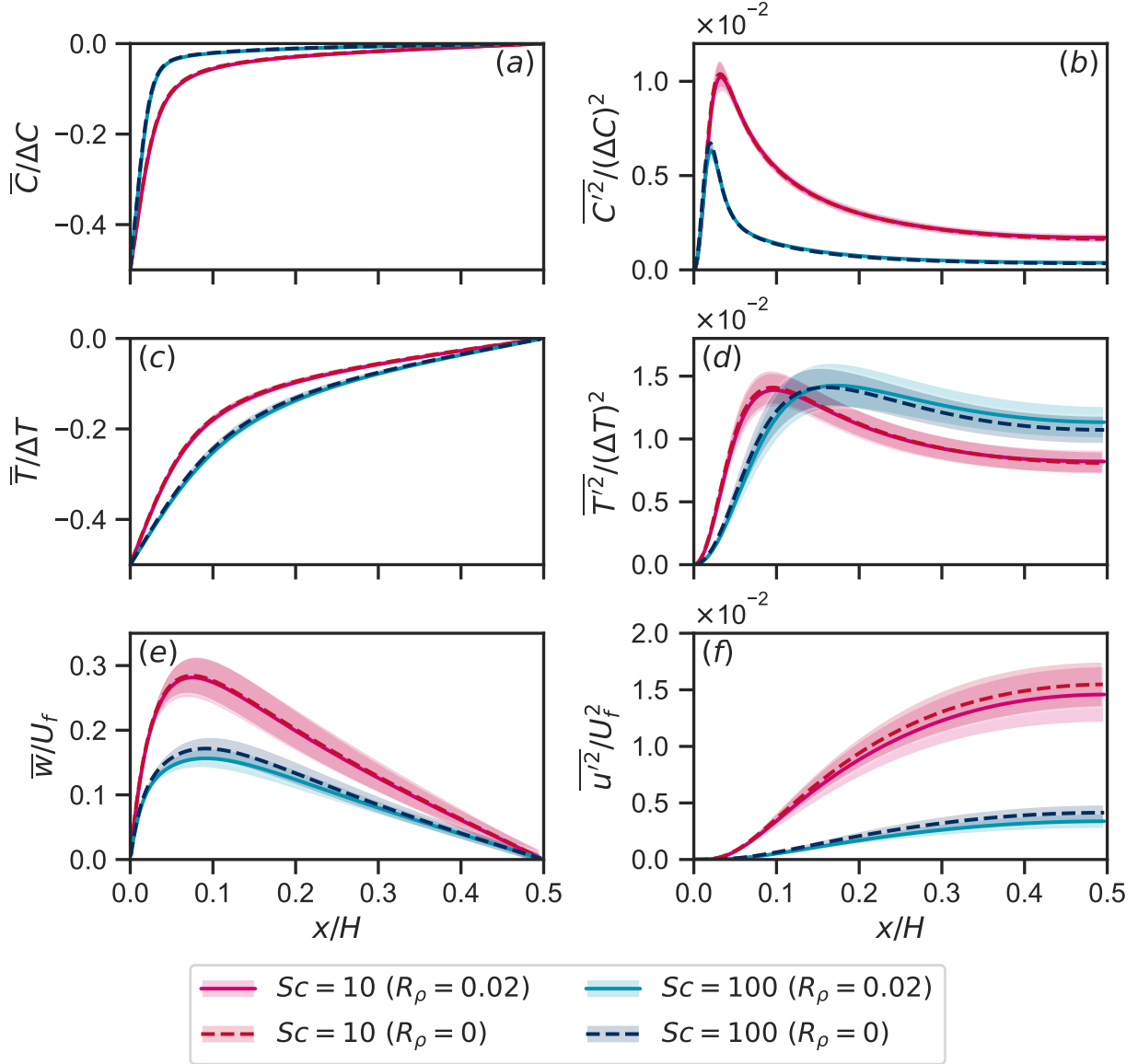


FIG. 1. Wall-normal profiles of flow quantities from simulations P10 (red dashed), A10L10 (pink), P100 (blue dashed), and A100L100 (cyan). Solid lines show the time-averaged profiles and the shaded regions highlight the standard deviation (in time) of the yz -averaged profiles. Quantities plotted are (a) mean concentration, (b) concentration variance, (c) mean temperature, (d) temperature variance, (e) mean vertical velocity, (f) wall-normal velocity variance.

density ratio R_ρ , the temperature field can impact the vertical velocity through the buoyancy force. A similar effect, although with a smaller impact, is observed in the $Sc = 10$ case, where the vertical velocity peak is slightly reduced in the case of an active temperature field. The reduction in peak velocity is also felt in the second order statistics plotted in the right

column of figure 1. Both cases with an active temperature field exhibit a slight decrease in the wall-normal kinetic energy in the bulk when compared to the passive cases. Curiously, the temperature variance in the bulk *increases* when the thermal buoyancy component is included. This may arise due to the marginally larger bulk temperature gradient in these simulations that would be in turn caused by the reduced mixing by the mean shear in the bulk.

Overall, although the effect of the thermal buoyancy component on the flow statistics is visible, it does not change the general picture describing the dynamics at $R_\rho = 0.02$. At this density ratio, the mean flow is driven by the buoyancy of the concentration field, and temperature is primarily transported as a passive scalar in this flow. We note here that in terms of a realistic ice-ocean scenario, $R_\rho = 0.02$ is even higher than what may be expected. Ocean salinity has a typical concentration of 35 g kg^{-1} , with the value of concentration at the ice face set by the dynamic three-equation boundary condition [7]. Kerr and McConnochie [15] performed experiments of a melting vertical ice face for ambient water temperatures between 0.3°C and 5.4°C , and estimated the interface salinity to vary between 1.9 g kg^{-1} and 24.5 g kg^{-1} . Using their measurements and theoretical predictions, we can estimate R_ρ by prescribing the haline contraction coefficient $\beta_C = 7.86 \times 10^{-4} (\text{g kg}^{-1})^{-1}$ and the thermal expansion coefficient $\beta_T = 3.87 \times 10^{-5} \text{ K}^{-1}$ from [20]. Although the true equation of state for seawater is nonlinear, and the effective thermal expansion coefficient varies with temperature, these values are reasonable for seawater with a high concentration of salt below 5°C . Despite the varying far-field temperatures in the experiments of [15], the density ratio from their results remains roughly constant across all the experiments at $R_\rho \approx 8 \times 10^{-3}$. Given that our results show the heat transport is primarily passive at $R_\rho = 0.02$, we expect this to also apply in oceanographically relevant flows.

B. Global heat flux

Since heat is transported like a passive scalar in our simulations, the mean flow velocity and salt flux are solely determined by the Rayleigh and Schmidt numbers as in single-component vertical convection. We refer to our previous work in [22] for further details on the parameter dependence of these quantities, and now turn to focus on the heat flux in the

system. We characterise the heat flux in terms of the thermal Nusselt number, defined

$$Nu_T = \frac{HF_T}{\kappa\Delta T} = \frac{H}{\Delta T} \left. \frac{\partial \bar{T}}{\partial x} \right|_{\text{wall}}, \quad (7)$$

where F_T is the mean diffusive heat flux at the walls.

When investigating the effect of differential diffusion on the heat flux, it is useful to consider the heat flux in terms of its ratio to the salt flux. If the Lewis number were equal to one, so heat and salt diffused at the same rates, then the governing equations (3) and (4) would become identical, and the heat and salt fluxes would therefore be equal. Defining an analogous Nusselt number Nu_C for salt concentration, we can investigate the dependence of the ratio $R = Nu_C/Nu_T$ on the Lewis number. This quantity is sometimes referred to as the boundary layer ratio [18] since $H/(2Nu)$ is a commonly used measure of scalar boundary layers. Some ice-ocean studies instead refer to the dimensionless flux ratio $\gamma = F_T\Delta C/F_C\Delta T$, which is directly related to R through $\gamma R = Le$ [30]. Both γ and R are equal to one when $Le = 1$.

We plot the Nusselt number ratio R measured from our simulations against the Lewis number in figure 2a. The passive temperature cases of set P overlay the active cases near-perfectly. For low Lewis numbers $Le \leq 1$, we find good agreement with a $1/3$ scaling law. This can be explained by our previous finding in [22] that the scalar flux in vertical convection at moderate Rayleigh number and high Schmidt number is consistent with $Nu_C \sim Re_\tau Sc^{1/3}$. Such a scaling with Sc is more widely applicable in high Schmidt number turbulent boundary layers [31], where the $Sc^{1/3}$ factor arises due to the scalar boundary layer being nested within the viscous sublayer [32]. Since temperature acts as a passive scalar in our simulations and $Pr \geq 1$ in all the cases we consider, we may expect an equivalent relationship as $Nu_T \sim Re_\tau Pr^{1/3}$. In this case, the Nusselt number ratio is $R \sim Le^{1/3}$. Since this scaling argument is consistent with the single-component VC results of [22], it should be valid at $Le = 1$, where we know that $R = 1$. For the scaling's range of validity, there should therefore be no pre-factor and we get $R = Le^{1/3}$.

However, as Le increases, the data deviates from the $1/3$ slope and the trend becomes steeper. This is most evident in the simulations with $Sc = 100$, where the effective scaling exponent of the data begins to approach $1/2$. Such a scaling has been used previously for convective boundary layers at vertical ice faces in [15]. An argument for this scaling was provided by Kerr [33], who considered the boundary layers at a horizontal ice face

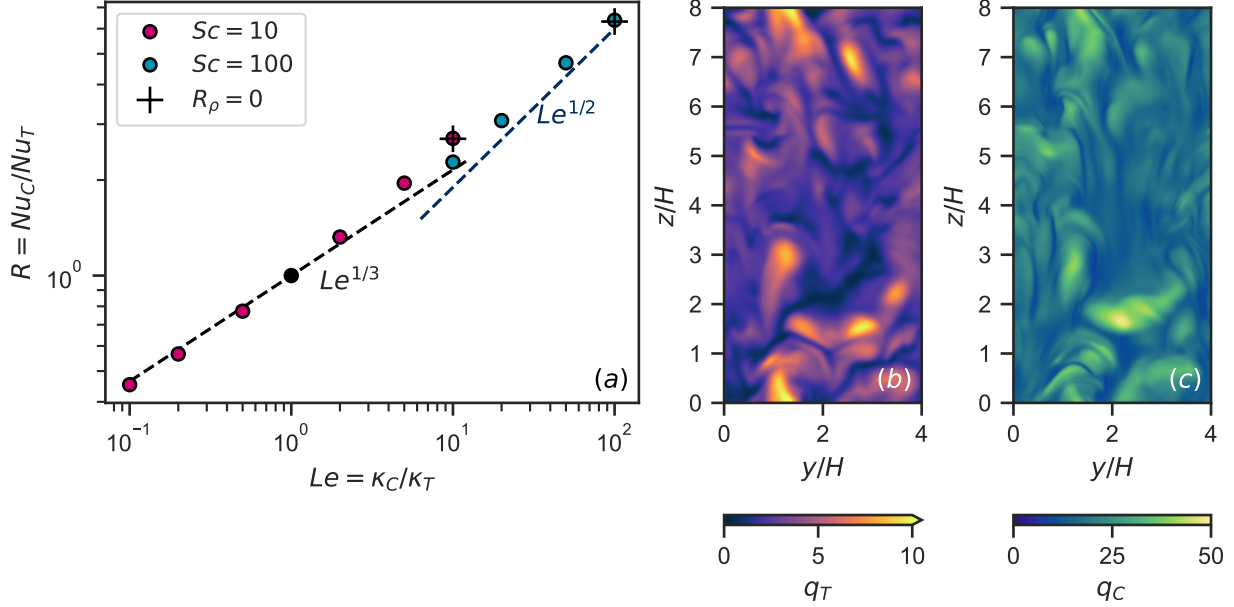


FIG. 2. (a) Ratio R of solutal Nusselt number Nu_C to thermal Nusselt number Nu_T across all the simulations plotted against the Lewis number. Colours denote the Schmidt number of the simulations, and crosses are used to highlight the cases with zero density ratio. The dashed straight lines with slopes $1/3$ and $1/2$ are shown for comparison. The black dot highlights the fixed theoretical point $R = Le = 1$. (b, c) Instantaneous snapshots of the local dimensionless heat and salt fluxes respectively at the wall $x = 0$ in simulation A100L100, where $Ra = 10^8$, $Sc = 100$, and $Le = 100$.

driving solutal convection in salt water above. In this scenario, the thermal and solutal boundary layers grow diffusively until the solutal boundary becomes convectively unstable. Thus the Nusselt numbers, which are inversely proportional to the boundary layer widths, evolve locally as $(\kappa t)^{-1/2}$ until they are intermittently reset by the convective instability. Throughout this diffusive phase, the Nusselt number ratio must therefore be $Le^{1/2}$.

C. Boundary layer analysis

To investigate whether the above arguments are suitable for describing the heat flux through the system, we now explicitly analyse the scalar boundary layers in the simulations. We define the width of the thermal boundary layer as follows in terms of the nature of the heat flux. Taking a yz -average of the advection-diffusion equation (3), assuming a

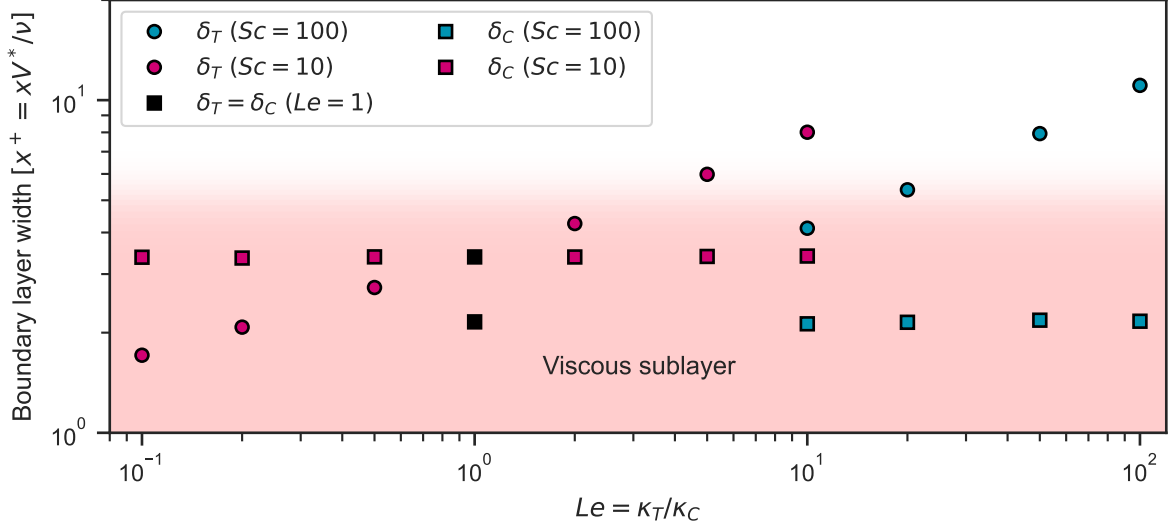


FIG. 3. Thermal (circles) and solutal (squares) boundary layer widths in viscous units plotted against the Lewis number. The viscous sublayer, defined as $x^+ \lesssim 5$, is highlighted by the red shading. Data points for $Le = 1$ (black squares) are inferred from the solutal boundary layer widths for each dataset (A10 and A100). For $Le = 1$ the thermal and solutal boundary layer widths must be equal.

statistically steady state, and integrating with respect to x shows us that the mean heat flux is uniform across all wall-normal locations:

$$F_T(x) = \underbrace{\kappa_T \frac{\partial \bar{T}}{\partial x}}_{\text{diffusive heat flux}} + \underbrace{\overline{-u'T'}}_{\text{turbulent heat flux}} = \text{constant}. \quad (8)$$

Here an overbar denotes an average with respect to y , z , and t , and a prime denotes the perturbation from this average. Far from the walls, the heat flux is dominated by its turbulent component and the mean temperature gradient is small. However, due to the no-penetration condition at the walls, heat flux at the boundaries must be purely diffusive. We therefore define the thermal boundary layer as the region where the diffusive flux is the dominant contribution to the heat flux. The boundary layer width is then defined as the crossover location of the fluxes:

$$\delta_T = x|_{\kappa \partial_x \bar{T} = -\overline{u'T'}}. \quad (9)$$

In figure 3 we plot the thermal boundary layer width in terms of the viscous wall unit $x^+ = xV^*/\nu$, where V^* is the friction velocity calculated from the mean shear stress at the wall. For the region $x^+ = O(1)$, viscous forces are dominant, and it is common to define

the viscous sublayer as $x^+ \lesssim 5$ in turbulent flows [34]. This sublayer is highlighted by the red shaded region in figure 3. Here, we also plot the solutal boundary layer width δ_C , which is defined in an analogous way to the thermal boundary layer width. The solutal boundary layer width δ_C is unaffected by the Lewis number, providing further evidence for the passive role of the temperature field. In both sets of simulations, $\delta_C^+ < 5$, i.e. the solutal boundary layer is nested within the viscous sublayer. As mentioned in the previous subsection, a nested scalar boundary layer is consistent with the scaling $Nu \sim Re_\tau Sc^{1/3}$, and so figure 3 provides some insight into why the data of [22] agrees with that relationship. For low Le , the thermal boundary layer is thinner than the solutal boundary layer and is therefore also nested within the viscous sublayer. When both thermal and solutal boundary layers are nested within the viscous one, we anticipate the flux ratio $R = Le^{1/3}$ observed for low Le in figure 2a.

Figure 3 also provides insight on why the deviations from the $Le^{1/3}$ flux ratio in figure 2a occur at different values of Le for the two different Schmidt numbers. For the Grashof number $Gr = 10^6$ considered in this study, the solutal boundary layer for $Sc = 100$ is nested deeper within the viscous sublayer than for $Sc = 10$. Assuming that $R = Le^{1/3}$ applies whenever both scalar boundary layers satisfy $\delta^+ < 5$, the Lewis number at which the thermal boundary layer reaches the edge of the viscous sublayer must therefore be larger for $Sc = 100$. Only once $\delta_T^+ > 5$ will we see a deviation from the $Nu_T \sim Re_\tau Pr^{1/3}$ scaling.

D. Turbulent diffusivity in the bulk

We conclude our analysis of the heat transport in the simulations by investigating the behaviour of the turbulent bulk away from the walls. In this region, the heat flux defined in (8) is dominated by the turbulent contribution. To gain insight into the transport properties of the bulk, we can rewrite (8) in terms of a turbulent diffusivity $K_T(x)$, such that

$$K_T(x) = -\frac{\overline{u'T'}}{\partial_x \overline{T}}, \quad F_T(x) = (\kappa_T + K_T(x)) \frac{\partial \overline{T}}{\partial x}. \quad (10)$$

We plot the wall-normal profiles of $K_T(x)$ for each of the simulations in sets A10 and A100 in figures 4a and 4b respectively. For each set, an equivalent profile of the turbulent salt diffusivity $K_C(x) = -\overline{u'C'}/\partial_x \overline{C}$ is also plotted for comparison and labelled as $Le = 1$. In all the simulations, we observe that the turbulent diffusivities are far greater than the molecular

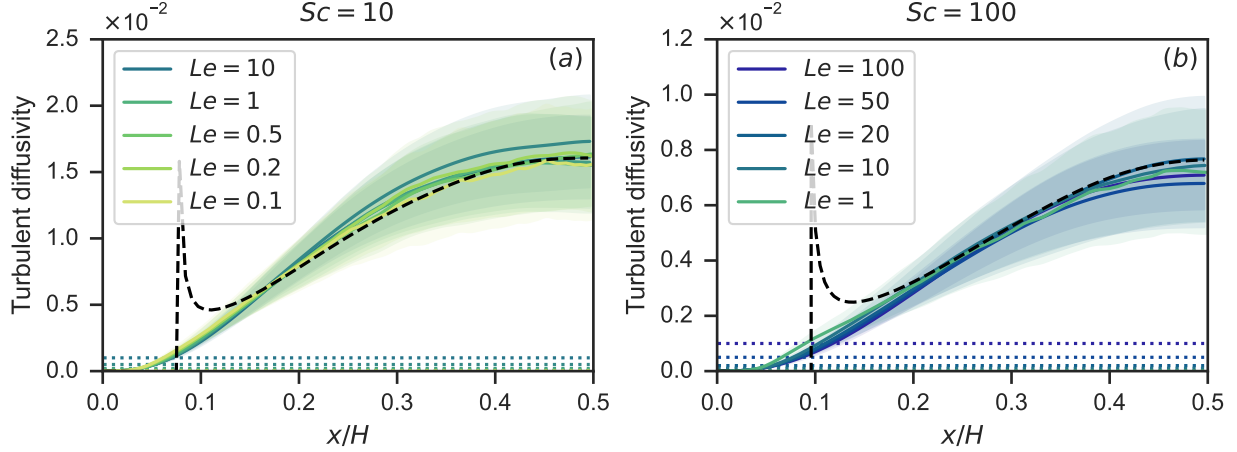


FIG. 4. Wall-normal profiles of the turbulent heat diffusivity K_T for each simulation, for two different Schmidt numbers, (a) $Sc = 10$ and (b) $Sc = 100$. Curves labelled as $Le = 1$ represent the turbulent diffusivity of the concentration field. For comparison, the wall-normal profile of the turbulent viscosity ν_t is also plotted as a dark dashed line, and the constant values of molecular diffusivity κ_T are plotted as dotted lines with colours matching the legend. Shaded regions highlight the temporal standard deviation of the turbulent heat flux $\overline{u'T'}$, normalised by the mean temperature gradient $\partial_x \overline{T}$ (multiplied by κ_T).

diffusivities away from the walls, and that the Lewis number has no significant effect on the profile of $K_T(x)$ in the bulk. The turbulence in the bulk thus mixes the temperature and concentration fields at an equal rate, and there are no double-diffusive effects on the mean profiles.

Furthermore, we find that the wall-normal momentum transport is also approximately equal to the scalar transport in the bulk. We quantify this by calculating the turbulent viscosity $\nu_t(x) = -\overline{u'w'}/\partial_x \overline{w}$, and also plotting it in figure 4 as black, dashed lines. The turbulent viscosity is negative close to the walls, and becomes ill-defined at the velocity extrema, so using a model based on a turbulent viscosity would be inappropriate for simulating this vertical convection flow. Nevertheless, ν_t agrees rather nicely with K_T in the bulk away from the velocity maximum. The heat transport in the bulk therefore satisfies $Pr_t \approx 1$, where $Pr_t = \nu_t/K_T$ is the turbulent Prandtl number. Indeed, convergence to $Pr_t \approx 1$ in uniformly sheared flow regions away from boundaries is frequently observed in a range of flows coupling shear and buoyancy effects [35–37].

IV. DISCUSSION AND CONCLUSIONS

In this study, we have investigated the effect of differential diffusion on the transport of heat and salt through a multicomponent fluid in vertical convection. For a density ratio of $R_\rho = 0.02$, relevant to the meltwater-driven convection at a vertical ice face in the ocean, we find that the convection is driven by differences in salt concentration, and that the contributions of the temperature to the buoyancy forcing are insignificant. Through comparison with the case of $R_\rho = 0$, where temperature is advected as a passive scalar, we conclude that classical double-diffusive phenomena such as salt fingers or diffusive convection are largely irrelevant in this flow geometry. This is further evidenced by the independence of the turbulent heat diffusivity in the bulk on the Lewis number. The heat transport away from the walls is characterised by a turbulent Prandtl number of $Pr_t \approx 1$, meaning that heat, salt, and momentum are all mixed at the same rate.

However, the difference in the molecular diffusivities of heat and salt, characterised by the Lewis number $Le = \kappa_C/\kappa_T$, is important in determining the relative fluxes of heat and salt through the system. When $Le < 1$, the ratio of salt flux to heat flux satisfies $R = Le^{1/3}$, but a steeper trend emerges as the Lewis number increases towards realistic values for salt water. This increase can be explained by the relative widths of the diffusive and viscous sublayers and their dependence on the Lewis number. Whenever both scalar boundary layers, defined as the regions where diffusive flux is larger than turbulent flux, are nested within the viscous sublayer, the scalar fluxes follow the classical high Pr scaling $Nu \sim Re_\tau Pr^{1/3}$ and the flux ratio therefore satisfies $R = Le^{1/3}$. As Le increases, the thermal sublayer can extend beyond the edge of the viscous sublayer, causing this prediction to break down. In this case the effective scaling exponent grows towards $1/2$, as suggested by [33] for diffusing boundary layers intermittently shed by instabilities.

Despite our enhanced understanding of the underlying physics for this boundary layer transition, predicting when this transition occurs for a given Ra and Sc unfortunately remains difficult. The key quantity that lacks a full description is the width of the diffusive solutal sublayer δ_C^+ relative to the viscous wall unit. Considering our previous work on high Sc vertical convection [22], there appears to be no simple relation linking the sublayer width and the two control parameters despite the simple configuration. We present the data from that single component work in figure 5.

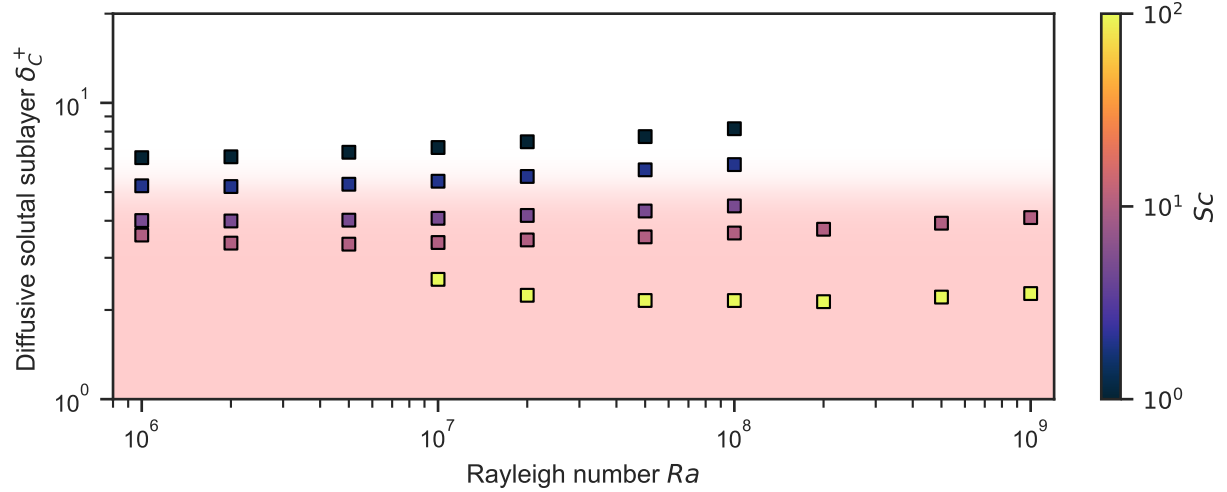


FIG. 5. Data from [22] showing the width of the diffusive solutal sublayer in viscous units $\delta_C^+ = \delta_C V^*/\nu$. The viscous sublayer $x^+ \lesssim 5$ is shaded in the same manner as in figure 3. No clear collapse of the data emerges: we observe smaller δ_C^+ for higher Sc , and a slight trend for δ_C^+ to increase with Ra at larger Ra . By the arguments of section III C, this would make the $Le^{1/2}$ flux ratio more appropriate for high Ra vertical convection, somewhat contradictory to the notion of a shear-driven boundary layer at high Ra .

Nevertheless, our results provide some new insight into the flux ratio at vertical ice-ocean interfaces. For the parameter range considered here, $Le^{1/3}$ appears to be a physical lower bound for the Nusselt number ratio R in low-density ratio vertical convection with heat and salt. This contrasts somewhat to previous results for diffusive convection underneath *horizontal* ice surfaces, where lower values of R are often inferred or theorized. For a Lewis number of $Le = 204$, Notz *et al.* [30] develop a theory describing the ablation of ‘false bottoms’ on the underside of ice floes, where the Nusselt number ratio is predicted to lie in the range $2.92 < R < 5.84$. Numerical studies of diffusive convection for Lewis numbers have shown that the dependence of R on Le appears to decrease as Le increases [19], contrary to our findings in figure 2. Of course, diffusive convection is a fundamentally different flow, where the mean buoyancy profile acts to suppress the flow and transport is due to double-diffusive processes. Extrapolating the two dashed lines from figure 2 out to this Lewis number gives a range of $5.88 < R < 8.57$ in the current study. The lower of these values, consistent with the shear-driven $Le^{1/3}$ prediction, is equivalent to a flux ratio of $\gamma = F_T/F_C = 35$ used in common ice-ocean parameterisations [9, 20].

TABLE II. Physical quantities related to the ice-water boundary condition.

λ [K(g kg ⁻¹)]	L/c_p [K]	C_∞ [g kg ⁻¹]	ν [m ² s ⁻¹]	κ_T [m ² s ⁻¹]	κ_C [m ² s ⁻¹]	β_C [(g kg ⁻¹) ⁻¹]
5.73×10^{-2}	84.0	34.5	1.95×10^{-6}	1.41×10^{-7}	8.02×10^{-10}	7.86×10^{-4}

Finally, we can consider how significant these discrepancies in the flux ratio can be for predictions of the melt rate at an ice-ocean interface. We use the three-equation boundary condition due to the salt-dependence of the melting point, and the conservation of heat and salt:

$$T_i + \lambda C_i = 0, \quad \frac{L}{c_p} \mathcal{V} = F_T, \quad C_i \mathcal{V} = F_C. \quad (11)$$

Here, T_i and C_i are the values of temperature and salt concentration at the ice-water interface, λ is the liquidus slope, L is the latent heat, c_p is the specific heat capacity, and \mathcal{V} is the ablation velocity, or melt rate, of the ice. For simplicity, we have neglected the heat flux contribution from conduction in the solid ice and consider the ice to be isothermal. Although latent heat is not considered directly in our simulations, from the second condition of (11) we note that the latent heat simply contributes to a constant scaling factor between the melt rate to the heat flux. If L/c_p is large, the melt rate is slow relative to the dynamics of the flow and we can assume our results for a stationary boundary will be relevant to the case of an evolving planar boundary. From (11), we can deduce that the Nusselt number ratio $R \propto F_C/F_T$ determines the interfacial salinity C_i through the quadratic equation

$$\frac{L}{c_p}(C_\infty - C_i) = \frac{Le}{R}C_i(T_\infty + \lambda C_i), \quad (12)$$

where T_∞ and C_∞ are the far-field values of temperature and concentration.

Using the physical parameter values in table II, we find that for an ambient ocean temperature of $T_\infty = 1^\circ\text{C}$, the interfacial salinity C_i varies significantly with the Nusselt number ratio R . For $Le = 175.8$, taking $R = Le^{1/3} = 5.6$ gives an interface salinity of $C_i = 19.3 \text{ g kg}^{-1}$, whereas following Kerr and McConnochie [15] and taking $R = Le^{1/2} = 13.25$ gives a result of $C_i = 24.9 \text{ g kg}^{-1}$. This in turn leads to an even greater effect on the melt rate. As a crude estimate for the salt flux, we can take the estimate $Nu_C \approx 0.1Ra^{1/3}$, although such a simple power-law description does not fully describe the vertical convection system [22]. Applying the values in table II leads to melt rate predictions from this simple model that vary from $\mathcal{V} = 35 \text{ m yr}^{-1}$ with $R = 13.25$ up to $\mathcal{V} = 84 \text{ m yr}^{-1}$ when using $R = 5.6$.

This factor of more than two in ablation velocity highlights the sensitive nature of melt parameterisations to the physical assumptions underlying them. More research is undoubtedly needed to couple numerical results and theory with experiments and observations. In particular, the transition between convectively-driven and shear-driven flows, where these different flux ratios appear relevant, must be understood. This has practical importance for the case in which steep ice faces are subject to horizontal flows in conjunction with the vertical convection of the meltwater - a case of mixed convection [12]. It will be useful to consider a variety of geometry in such process studies. This work focused on the symmetric case of a vertical channel to obtain temporally converged statistics, but it is unclear how exactly the lateral confinement imposed by the walls may affect the boundary layers when compared to a growing wall plume [37, 38]. In environmental scenarios, the ice surface is also rarely smooth, with distinctive scallop-like roughness seemingly ubiquitous on the underside of icebergs [39]. A full understanding of the ice-ocean boundary layer will be incomplete without a physical description of this complex two-way coupling between the flow and the shape evolution of the solid phase.

Appendix A: Temperature variance budget

As an extension to the heat flux analysis in section III, where we consider the budget terms for the mean temperature equation, we can investigate the terms contributing to the evolution of the temperature variance. This informs us about the mechanisms driving, transporting and dissipating turbulent thermal fluctuations through the system. We begin by decomposing the temperature field as before into a mean component and its fluctuation, where the mean is taken in the homogeneous directions y and z :

$$T(x, y, z, t) = \bar{T}(x, t) + T'(x, y, z, t). \quad (\text{A1})$$

By multiplying (3) by T and decomposing the temperature field as above, we can derive the evolution equation for the temperature variance as

$$\frac{\partial}{\partial t} \frac{\overline{T'^2}}{2} = \kappa \frac{\partial^2}{\partial x^2} \frac{\overline{T'^2}}{2} - \frac{\partial}{\partial x} \overline{u' \frac{T'^2}{2}} - \overline{u' T'} \frac{\partial \bar{T}}{\partial x} - \kappa \overline{|\nabla T'|^2}, \quad (\text{A2})$$

$$= \mathcal{D} + \mathcal{T} + \mathcal{P} - \varepsilon_T. \quad (\text{A3})$$

The budget terms on the right hand side can be interpreted respectively as the diffusion and transport of temperature variance, the production of temperature variance by the mean

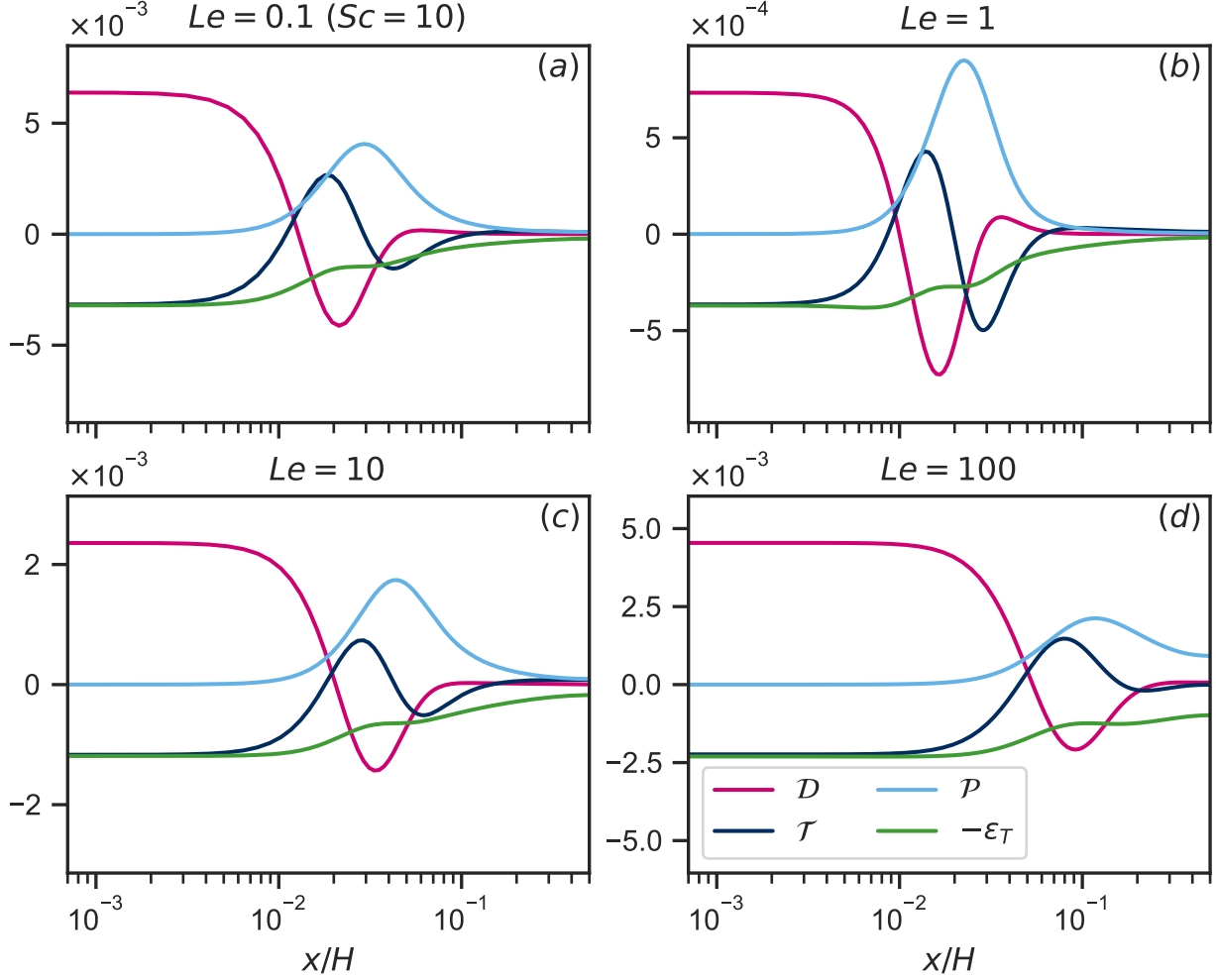


FIG. 6. Wall-normal profiles of the scalar variance budget terms from (A3) for three simulations: (a) A10L01 (b, c) A100L10 (d) A100L100. In (a, c, d) the temperature variance budget is presented. In (b) the budget terms plotted are actually those of the concentration variance to provide insight into the dynamics at $Le = 1$, in which case temperature statistics would evolve identically to the concentration statistics shown in panel (b).

temperature gradient, and the dissipation of temperature variance. Since the system reaches a statistically steady state, the budget terms must sum to zero at every wall-normal position. We also note that the volume integrals of the transport and diffusion terms \mathcal{T} and \mathcal{D} must be zero, so globally there is a simple balance between production \mathcal{P} and dissipation ε_T .

In figure 6 we plot the various budget terms as a function of x for a selection of simulations at various Lewis numbers. Overall, the structure of the budgets appears very similar in all these cases. The production is localised with a distinctive peak, but this is not balanced

locally by dissipation. Instead, there are also significant negative contributions from the diffusion and transport terms. We can use figure 1(b,d) to provide further interpretation for the location of the production peak. In that figure, we observe a peak in the temperature (and concentration) variance that moves further from the wall as Le increases. This variance peak coincides with the minimum of the diffusion term in figure 6, which is slightly closer to the wall than the peak in variance production. In the bulk, the various budget terms are small at low Le , but as Le increases and the production peak moves further from the walls, the production and dissipation at the channel centre become more significant. Despite the localised peak in variance production away from the wall, the peak value of its dissipation occurs at the wall as $x \rightarrow 0$. Here the transport and dissipation terms are equal and opposite, balancing the contribution from diffusion in every simulation. In this near-wall sublayer region, these quantities are roughly constant, suggesting that the rms temperature fluctuation scales linearly with distance from the wall.

ACKNOWLEDGMENTS

This project has received funding from the European Research Council (ERC) under the European Union’s Horizon 2020 research and innovation programme (Grant agreement No. 804283). We acknowledge PRACE for awarding us access to MareNostrum at Barcelona Supercomputing Center (BSC), Spain (Project 2020235589). This work was also carried out on the Dutch national e-infrastructure with the support of SURF Cooperative.

-
- [1] J. Mouginot, E. Rignot, A. A. Bjørk, M. van den Broeke, R. Millan, M. Morlighem, B. Noël, B. Scheuchl, and M. Wood, Forty-six years of Greenland Ice Sheet mass balance from 1972 to 2018, *Proc. Natl. Acad. Sci.* **116**, 9239 (2019).
 - [2] E. Rignot, J. Mouginot, B. Scheuchl, M. van den Broeke, M. J. van Wessem, and M. Morlighem, Four decades of Antarctic Ice Sheet mass balance from 1979–2017, *Proc. Natl. Acad. Sci.* **116**, 1095 (2019).
 - [3] H. Goelzer, S. Nowicki, A. Payne, E. Larour, H. Seroussi, W. H. Lipscomb, J. Gregory, A. Abe-Ouchi, A. Shepherd, E. Simon, C. Agosta, P. Alexander, A. Aschwanden, A. Barthel, R. Calov, C. Chambers, Y. Choi, J. Cuzzone, C. Dumas, T. Edwards, D. Felikson, X. Fettweis, N. R.

- Golledge, R. Greve, A. Humbert, P. Huybrechts, S. Le clec'h, V. Lee, G. Leguy, C. Little, D. P. Lowry, M. Morlighem, I. Nias, A. Quiquet, M. Rückamp, N.-J. Schlegel, D. A. Slater, R. S. Smith, F. Straneo, L. Tarasov, R. van de Wal, and M. van den Broeke, The future sea-level contribution of the Greenland ice sheet: A multi-model ensemble study of ISMIP6, *The Cryosphere* **14**, 3071 (2020).
- [4] H. Seroussi, S. Nowicki, A. J. Payne, H. Goelzer, W. H. Lipscomb, A. Abe-Ouchi, C. Agosta, T. Albrecht, X. Asay-Davis, A. Barthel, R. Calov, R. Cullather, C. Dumas, B. K. Galton-Fenzi, R. Gladstone, N. R. Golledge, J. M. Gregory, R. Greve, T. Hattermann, M. J. Hoffman, A. Humbert, P. Huybrechts, N. C. Jourdain, T. Kleiner, E. Larour, G. R. Leguy, D. P. Lowry, C. M. Little, M. Morlighem, F. Pattyn, T. Pelle, S. F. Price, A. Quiquet, R. Reese, N.-J. Schlegel, A. Shepherd, E. Simon, R. S. Smith, F. Straneo, S. Sun, L. D. Trusel, J. Van Breedam, R. S. W. van de Wal, R. Winkelmann, C. Zhao, T. Zhang, and T. Zwinger, ISMIP6 Antarctica: A multi-model ensemble of the Antarctic ice sheet evolution over the 21st century, *The Cryosphere* **14**, 3033 (2020).
- [5] T. L. Edwards, S. Nowicki, B. Marzeion, R. Hock, H. Goelzer, H. Seroussi, N. C. Jourdain, D. A. Slater, F. E. Turner, C. J. Smith, C. M. McKenna, E. Simon, A. Abe-Ouchi, J. M. Gregory, E. Larour, W. H. Lipscomb, A. J. Payne, A. Shepherd, C. Agosta, P. Alexander, T. Albrecht, B. Anderson, X. Asay-Davis, A. Aschwanden, A. Barthel, A. Bliss, R. Calov, C. Chambers, N. Champollion, Y. Choi, R. Cullather, J. Cuzzzone, C. Dumas, D. Felikson, X. Fettweis, K. Fujita, B. K. Galton-Fenzi, R. Gladstone, N. R. Golledge, R. Greve, T. Hattermann, M. J. Hoffman, A. Humbert, M. Huss, P. Huybrechts, W. Immerzeel, T. Kleiner, P. Kraaijenbrink, S. Le clec'h, V. Lee, G. R. Leguy, C. M. Little, D. P. Lowry, J.-H. Malles, D. F. Martin, F. Maussion, M. Morlighem, J. F. O'Neill, I. Nias, F. Pattyn, T. Pelle, S. F. Price, A. Quiquet, V. Radić, R. Reese, D. R. Rounce, M. Rückamp, A. Sakai, C. Shafer, N.-J. Schlegel, S. Shannon, R. S. Smith, F. Straneo, S. Sun, L. Tarasov, L. D. Trusel, J. Van Breedam, R. van de Wal, M. van den Broeke, R. Winkelmann, H. Zekollari, C. Zhao, T. Zhang, and T. Zwinger, Projected land ice contributions to twenty-first-century sea level rise, *Nature* **593**, 74 (2021).
- [6] L. Favier, N. C. Jourdain, A. Jenkins, N. Merino, G. Durand, O. Gagliardini, F. Gillet-Chaulet, and P. Mathiot, Assessment of sub-shelf melting parameterisations using the ocean–ice-sheet coupled model NEMO(v3.6)–Elmer/Ice(v8.3), *Geosci. Model Dev.* **12**, 2255 (2019).
- [7] S. Martin and P. Kauffman, An Experimental and Theoretical Study of the Turbulent and

- Laminar Convection Generated under a Horizontal Ice Sheet Floating on Warm Salty Water, *J. Phys. Oceanogr.* **7**, 272 (1977).
- [8] A. Malyarenko, A. J. Wells, P. J. Langhorne, N. J. Robinson, M. J. M. Williams, and K. W. Nicholls, A synthesis of thermodynamic ablation at ice–ocean interfaces from theory, observations and models, *Ocean Model.* **154**, 101692 (2020).
 - [9] D. M. Holland and A. Jenkins, Modeling Thermodynamic Ice–Ocean Interactions at the Base of an Ice Shelf, *J. Phys. Oceanogr.* **29**, 1787 (1999).
 - [10] S. Kimura, K. W. Nicholls, and E. Venables, Estimation of Ice Shelf Melt Rate in the Presence of a Thermohaline Staircase, *J. Phys. Oceanogr.* **45**, 133 (2015).
 - [11] L. Middleton, P. E. D. Davis, J. R. Taylor, and K. W. Nicholls, Double Diffusion As a Driver of Turbulence in the Stratified Boundary Layer Beneath George VI Ice Shelf, *Geophys. Res. Lett.* **49**, e2021GL096119 (2022).
 - [12] R. H. Jackson, J. D. Nash, C. Kienholz, D. A. Sutherland, J. M. Amundson, R. J. Motyka, D. Winters, E. Skyllingstad, and E. C. Pettit, Meltwater Intrusions Reveal Mechanisms for Rapid Submarine Melt at a Tidewater Glacier, *Geophys. Res. Lett.* **47**, e2019GL085335 (2020).
 - [13] P. Dutrieux, C. Stewart, A. Jenkins, K. W. Nicholls, H. F. J. Corr, E. Rignot, and K. Steffen, Basal terraces on melting ice shelves, *Geophys. Res. Lett.* **41**, 5506 (2014).
 - [14] I. J. Hewitt, Subglacial Plumes, *Annu. Rev. Fluid Mech.* **52**, 145 (2020).
 - [15] R. C. Kerr and C. D. McConnochie, Dissolution of a vertical solid surface by turbulent compositional convection, *J. Fluid Mech.* **765**, 211 (2015).
 - [16] C. D. McConnochie and R. C. Kerr, Dissolution of a sloping solid surface by turbulent compositional convection, *J. Fluid Mech.* **846**, 563 (2018).
 - [17] C. A. Vreugdenhil and J. R. Taylor, Stratification Effects in the Turbulent Boundary Layer beneath a Melting Ice Shelf: Insights from Resolved Large-Eddy Simulations, *J. Phys. Oceanogr.* **49**, 1905 (2019).
 - [18] M. G. Rosevear, B. Gayen, and B. K. Galton-Fenzi, The role of double-diffusive convection in basal melting of Antarctic ice shelves, *PNAS* **118**, 10.1073/pnas.2007541118 (2021).
 - [19] T. Keitzl, J. P. Mellado, and D. Notz, Reconciling estimates of the ratio of heat and salt fluxes at the ice–ocean interface, *J. Geophys. Res. Oceans* **121**, 8419 (2016).
 - [20] A. Jenkins, Convection-Driven Melting near the Grounding Lines of Ice Shelves and Tidewater Glaciers, *J. Phys. Oceanogr.* **41**, 2279 (2011).

- [21] B. Gayen, R. W. Griffiths, and R. C. Kerr, Simulation of convection at a vertical ice face dissolving into saline water, *J. Fluid Mech.* **798**, 284 (2016).
- [22] C. J. Howland, C. S. Ng, R. Verzicco, and D. Lohse, Boundary layers in turbulent vertical convection at high Prandtl number, *J. Fluid Mech.* **930**, A32 (2022).
- [23] O. S. Kerr and K. Y. Tang, Double-diffusive instabilities in a vertical slot, *J. Fluid Mech.* **392**, 213 (1999).
- [24] S. Xin, P. Le Quéré, and L. S. Tuckerman, Bifurcation analysis of double-diffusive convection with opposing horizontal thermal and solutal gradients, *Phys. Fluids* **10**, 850 (1998).
- [25] C. Beaume, A. M. Rucklidge, and J. Tumelty, Near-onset dynamics in natural doubly diffusive convection, *J. Fluid Mech.* **934**, 10.1017/jfm.2021.1121 (2022).
- [26] R. Verzicco and P. Orlandi, A Finite-Difference Scheme for Three-Dimensional Incompressible Flows in Cylindrical Coordinates, *J. Comput. Phys.* **123**, 402 (1996).
- [27] E. P. van der Poel, R. Ostilla-Mónico, J. Donners, and R. Verzicco, A pencil distributed finite difference code for strongly turbulent wall-bounded flows, *Computers & Fluids* **116**, 10 (2015).
- [28] R. Ostilla-Monico, Y. Yang, E. P. van der Poel, D. Lohse, and R. Verzicco, A multiple-resolution strategy for Direct Numerical Simulation of scalar turbulence, *J. Comput. Phys.* **301**, 308 (2015).
- [29] O. Shishkina, R. J. A. M. Stevens, S. Grossmann, and D. Lohse, Boundary layer structure in turbulent thermal convection and its consequences for the required numerical resolution, *New J. Phys.* **12**, 075022 (2010).
- [30] D. Notz, M. G. McPhee, M. G. Worster, G. A. Maykut, K. H. Schlünzen, and H. Eicken, Impact of underwater-ice evolution on Arctic summer sea ice, *J. Geophys. Res. Oceans* **108**, 10.1029/2001JC001173 (2003).
- [31] B. A. Kader and A. M. Yaglom, Heat and mass transfer laws for fully turbulent wall flows, *Int. J. Heat Mass Tran.* **15**, 2329 (1972).
- [32] H. Schlichting and K. Gersten, *Boundary-Layer Theory*, ninth ed. (Springer, Berlin, Heidelberg, 2016).
- [33] R. C. Kerr, Dissolving driven by vigorous compositional convection, *J. Fluid Mech.* **280**, 287 (1994).
- [34] P. Davidson, *Turbulence: An Introduction for Scientists and Engineers*, second edition ed. (Oxford University Press, Oxford, New York, 2015).

- [35] D. Chung and G. Matheou, Direct numerical simulation of stationary homogeneous stratified sheared turbulence, *J. Fluid Mech.* **696**, 434 (2012).
- [36] G. D. Portwood, S. M. de Bruyn Kops, and C. P. Caulfield, Asymptotic Dynamics of High Dynamic Range Stratified Turbulence, *Phys. Rev. Lett.* **122**, 194504 (2019).
- [37] M. van Reeuwijk, M. Holzner, and C. P. Caulfield, Mixing and entrainment are suppressed in inclined gravity currents, *J. Fluid Mech.* **873**, 786 (2019).
- [38] J. Ke, N. Williamson, S. W. Armfield, A. Komiya, and S. E. Norris, High Grashof number turbulent natural convection on an infinite vertical wall, *J. Fluid Mech.* **929**, 10.1017/jfm.2021.839 (2021).
- [39] M. Bushuk, D. M. Holland, T. P. Stanton, A. Stern, and C. Gray, Ice scallops: A laboratory investigation of the ice–water interface, *J. Fluid Mech.* **873**, 942 (2019).